

Low-Loss Zero-Index Materials

Haoning Tang,^{||} Clayton DeVault,^{||} Sarah Alejandra Camayd-Muñoz, Yueyang Liu, Danchen Jia, Fan Du, Olivia Mello, Daryl I. Vulis, Yang Li,^{*} and Eric Mazur^{*}



Cite This: *Nano Lett.* 2021, 21, 914–920



Read Online

ACCESS |



Metrics & More



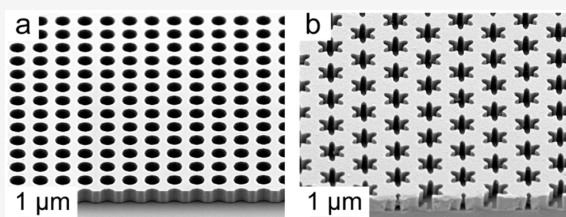
Article Recommendations



Supporting Information

ABSTRACT: Materials with a zero refractive index support electromagnetic modes that exhibit stationary phase profiles. While such materials have been realized across the visible and near-infrared spectral range, radiative and dissipative optical losses have hindered their development. We reduce losses in zero-index, on-chip photonic crystals by introducing high-*Q* resonances via resonance-trapped and symmetry-protected states. Using these approaches, we experimentally obtain quality factors of 2.6×10^3 and 7.8×10^3 at near-infrared wavelengths, corresponding to an order-of-magnitude reduction in propagation loss over previous designs. Our work presents a viable approach to fabricate zero-index on-chip nanophotonic devices with low-loss.

KEYWORDS: Zero-Index, photonic crystal, bound state in the continuum, integrated photonics



INTRODUCTION

Zero-index materials have generated substantial interest in recent years because of their electromagnetic modes that exhibit stationary phase profiles. These modes permit subwavelength confinement,^{1,2} enhanced nonlinearities,^{3–8} and extended quantum coherence,^{9,10} opening the door to many interesting applications. Particular metal oxide films, such as indium tin oxide and aluminum-doped zinc oxide, and metal–dielectric metamaterials exhibit near-zero index behavior at optical and near-infrared wavelength;^{11,12} however, these systems have large optical losses and high impedance, which hinders the study of near-zero index phenomena and is detrimental to applications. All-dielectric photonic crystals (PhCs) eliminate metallic dissipative losses and can support a zero-index mode at $k = 0$; in addition they have finite impedance and are compatible with nanophotonic integrated circuits.^{13–15} These properties are particularly important for on-chip nonlinear and quantum devices where long-range, stationary phase profiles are required.^{16,17}

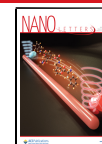
The zero-index properties of a PhC originate from a triple mode degeneracy resulting in an accidental Dirac cone located at the gamma-point of the Brillouin zone.^{13,18} Although material loss in an all-dielectric PhC is negligible, the zero-index modes are above the light-line causing substantial radiative losses both in- and out-of-plane. In-plane radiative losses can be mitigated using photonic bandgap structures, but earlier attempts¹⁴ to reduce out-of-plane radiative losses using metallic boundaries introduce ohmic dissipation. Consequently, loss appears to be a common challenge for all zero-index materials, and novel solutions are required for zero-index phenomena and applications to come to fruition.

We substantially reduced radiative losses in near-infrared zero-index dielectric photonic crystals by increasing the quality factor (*Q*-factor) using two different approaches. The first approach achieves a high *Q*-factor by introducing resonance-trapped^{19–21} modes with out-of-plane far-field destructive interference. The second approach realizes a high *Q* via symmetry-protected modes. Both approaches originate from bound states in the continuum;²² however, the on-chip design breaks the out-of-plane mirror symmetry and the *Q*-factor will remain finite.²³ The devices no longer have an infinite lifetime. Characterized by an infinite *Q*-factor, these states remain bound despite having an energy-momentum state which exists in the continuum of radiation. We show an improvement in quality factor and reduction in propagation loss by an order of magnitude over previous PhC Dirac cone designs. Despite a high *Q*-factor, the zero-index PhC's impedance remains finite due to both the effective permittivity and permeability approaching zero at the same wavelength.¹⁴ With the appropriate low-loss dielectric, such as silicon and titanium oxide, our designs operate across a broad range of visible and infrared frequencies, making them versatile designs for realizing low-loss on-chip zero-index applications and devices.

Received: September 3, 2020

Revised: November 23, 2020

Published: January 5, 2021



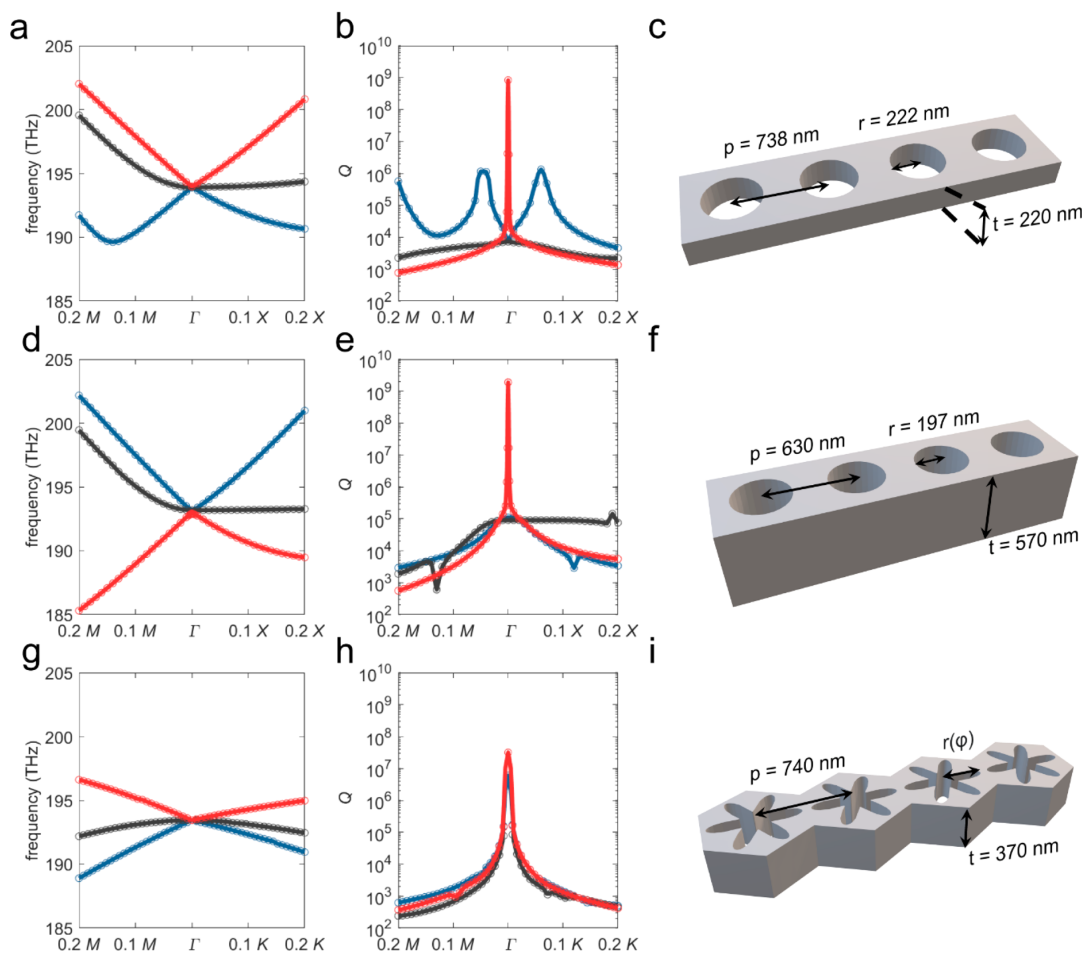


Figure 1. Reducing radiation losses using resonance-trapped and symmetry-protected designs. Band structure (left), quality factor (middle), and device geometry (right) for lossy (top), resonance-trapped (middle) and symmetry-protected (bottom) zero-index PhC designs. The colors in the band structure and quality factor plots correspond to distinct modes. For the lossy and resonance-trapped PhC designs, the red curves correspond to quadrupole modes, while the blue and black curves correspond to dipole modes. For the symmetry-protected PhC design, the modes are more complex (see Supporting Information Figure S1).

DISCUSSION

Our previously published, lossy zero-index PhC design consists of a square array with a 738 nm pitch of air holes of radius 222 nm in a 220 nm-thick silicon film deposited on a silicon oxide insulator substrate (Figure 1c).¹⁵ Using numerical finite element modeling, we determined the band structure (Figure 1a) and the Q -factor (Figure 1b). The band structure near the Γ -point consists of three degenerate quasi-TE modes that have approximately linear dispersion and form an accidental Dirac cone at a wavelength of 1550 nm. At the Γ -point, the modes are classified as a degenerate pair of dipole modes and a single quadrupole mode. The Q -factor of the two dipole modes is 7.3×10^3 while the Q -factor of the quadrupole mode is 8.3×10^8 , which shows that the dipole modes dominate the contribution to the structure's radiative losses.

To suppress radiative loss of the Dirac-cone modes we used two approaches to increase the Q -factor while retaining a Dirac-cone dispersion. The first approach involves increasing the thickness of the silicon slab to introduce a resonance-trapped dipole mode. The on-resonance condition for this

design corresponds to total destructive interference between the doubly degenerate dipole modes and additional on- Γ modes radiating from the photonic crystal slab.^{19–21,24,25} We optimized (see Supporting Information Figure S2 and Figure S3) the airhole radius, array pitch, and slab thickness to obtain both a Dirac cone and a high- Q resonance at 1550 nm, yielding a geometry of $r = 197$ nm; $p = 630$ nm; $t = 570$ nm (Figure 1f). The geometry yields a degenerate Dirac cone dispersion at 1550 nm (Figure 1d) with a dipole mode Q -factor of 9.0×10^4 , an order of magnitude larger than that in the lossy design (Figure 1e).

The second approach involves symmetry-protected modes,²⁶ obtained in a hexagonal lattice of flower-shaped air-holes represented by an airhole radius $r(\phi) = r_0 + r_d(6\phi)$ with $r_0 = 226.4$ nm and $r_d = 109$ nm, a unit-cell pitch of $p = 740$ nm, and a slab thickness of $t = 370$ nm (Figure 1i). The hexagonal lattice belongs to the C_{6v} point group and supports an irreducible representation of quasi-TM modes which do not couple to plane waves at normal incidence because their symmetry is incompatible with plane waves at the Γ -point.²⁷ Figure 1g,h shows the calculated dispersion and Q -factors for the three

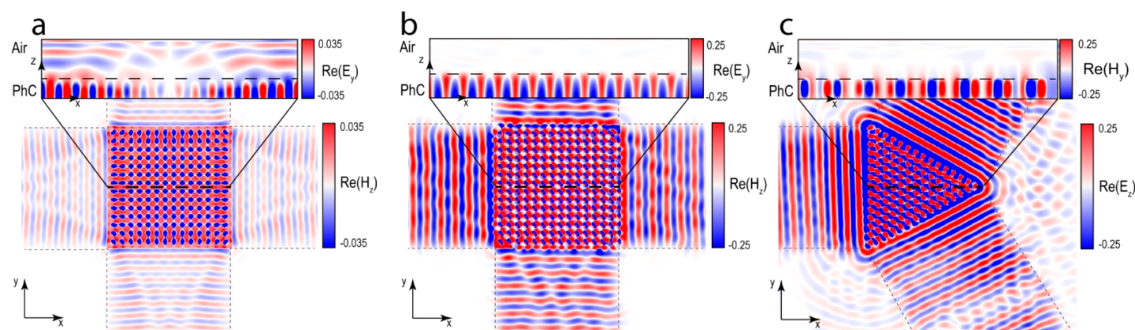


Figure 2. Electromagnetic field patterns in zero-index materials. In-plane field patterns and radiative field patterns (inset) in lossy (left), resonance-trapped (middle), and symmetry-protected (right) zero-index PhC designs excited by dipole sources. In the in-plane direction, the waves are emitted from the PhC slabs into SU-8 waveguides; in the out-of-plane direction, the waves are radiated into air. The polarization modes are quasi-TE for lossy (left) and resonance-trapped (middle) zero-index PhC, and quasi-TM for symmetry-protected (right) zero-index PhC.

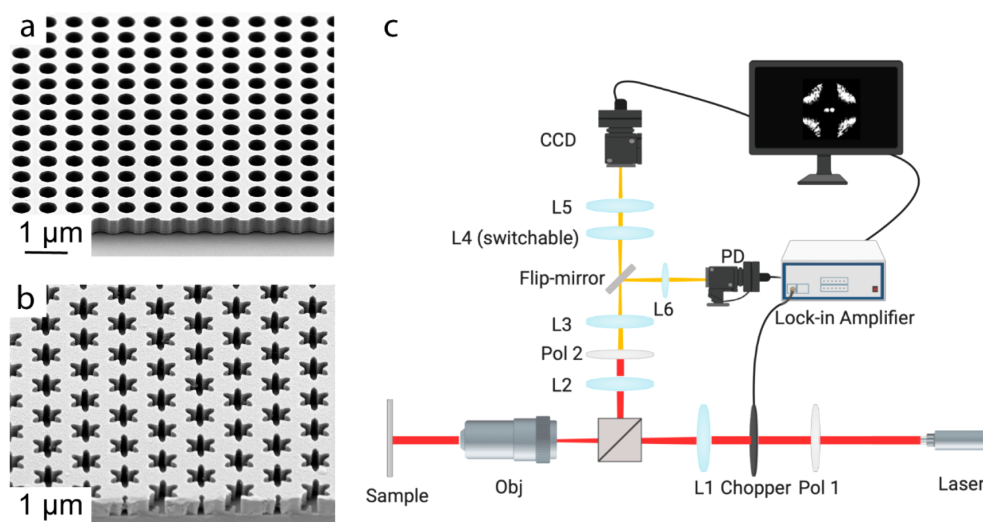


Figure 3. Device and experimental setup. Scanning electron microscopy images of the (a) resonance-trapped and (b) symmetry-protected PhC devices. The total patterned area is approximately $500 \times 500 \mu\text{m}^2$. (c) Setup for measuring iso-frequency contours. A collimated laser is first polarized and then focused by lens (L1) with focal length $f = +15 \text{ cm}$ (L1) onto the back focal plane of a $10\times$ infinity-corrected NIR objective, so the sample is illuminated by a collimated beam. The angle of incidence is controlled by moving L1 in the horizontal plane to achieve resonance coupling at each excitation wavelength. We image the back focal plane of the objective onto the CCD camera using a $1.67\times$ -magnification $4f$ -relay lens system. Lens L4 can be removed to switch the setup to real-space imaging for initial alignment.

modes in this symmetry-protected PhC design across the relevant portion of the Brillouin zone. The modes form a Dirac cone dispersion with minimum Q -factor of 6.0×10^6 , which is 3 orders of magnitude larger than the lossy design.

Figure 2 shows the in-plane and out-of-plane (insets) field profiles of the three zero-index designs. For each design, the photonic crystal's interfaces are connected to SU-8 waveguides. We numerically compute the field profiles by exciting the zero-index mode of the three structures with in-phase dipole sources located in each unit cell. All three structures support zero-index modes leading to highly directional in-plane emission into the SU-8 waveguides, facilitated by the nonzero group velocity and finite impedance of Dirac cone structures (see Supporting Information Figure S5 and Figure S6). We calculate the radiative losses factor in each design by normalizing the radiative power to the guided mode's power. At the zero-index wavelength, the lossy structure shows significant leakage of radiation in the out-of-plane direction (Figure 2a inset),

corresponding to a radiative loss factor of 77.8%. Radiative modes are suppressed in the resonance-trapped PhC design (Figure 2b inset, 46.5% radiative loss factor) and further suppressed in the symmetry-protected design (Figure 2c inset, 26.5% radiative loss factor). The small amount of leakage radiation visible in Figure 2b,c is due to direct radiation from the dipole sources.

To verify our numerical findings, we fabricated the lossy, resonance-trapped PhC and symmetry-protected PhC designs in an SOI wafer with a 220 nm thick silicon device layer. To obtain the thicknesses required for the resonance-trapped (570 nm) and symmetry-protected (370 nm) designs, we used chemical vapor deposition to deposit amorphous silicon on top of the device layer; the index contrast between the crystalline silicon and deposited amorphous silicon is small (~ 0.01). The airhole patterns were then defined using conventional electron-beam lithography methods. Scanning electron images of the

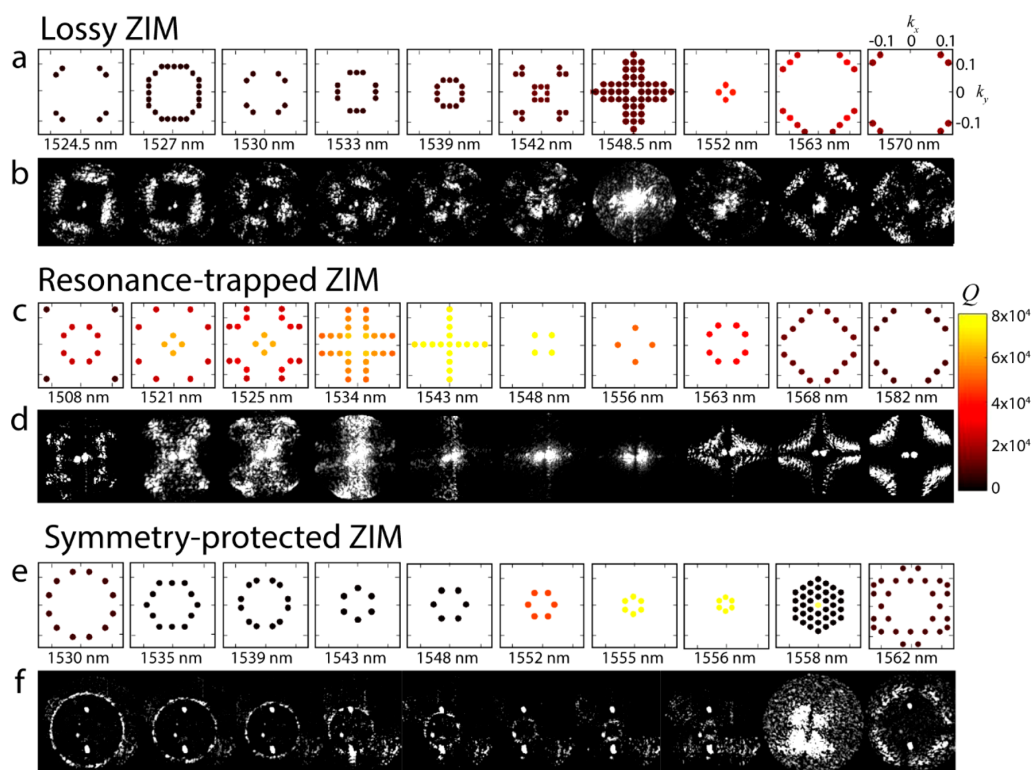


Figure 4. Contour images. Numerical (a,c,e) and measured (b,d,f) iso-frequency contours of lossy (top), resonance-trapped (middle), and symmetry-protected (bottom) zero-index PhC devices. The color scale indicates the calculated Q -factor. In the measured images, the contrast is normalized to improve visibility. The pair of bright spots visible in many of the measured images are the laser's incident and reflected beam.

resonance-trapped and symmetry-protected PhCs are shown in Figure 3a,b, respectively.

To determine the zero-index wavelength of our PhC devices, we used the Fourier microscope setup shown in Figure 3c to image the isofrequency contours²⁸ of our three devices (lossy, resonance-trapped PhC, and symmetry-protected PhC designs). Each device is illuminated with a polarized and collimated tunable (1500–1630 nm) laser beam using a near-infrared 10X objective. For a given wavelength, we adjust the incidence angle to match the momentum of a particular resonant mode. Light from this resonant mode is then scattered by fabrication disorder (e.g., roughness, lattice imperfections, pattern errors) into modes with similar momentum, which then radiate to form isofrequency contours in the far-field.²⁸ We remove the incident laser beam using a second polarizer (Supporting Information Figure S7) and then image the contours onto a CCD camera.

Figure 4 shows the measured and calculated isofrequency contours of the three samples. The color scale represents the numerically calculated Q -factor of each contour. For clarity, we normalize the intensity of the CCD contour images because the scattered intensity approaches zero for high- Q contours. The lossy PhC design supports quasi-TE resonances with low- Q dipole modes below the Dirac point wavelength of 1549.0 nm. In the experimental images (Figure 4b), we see bright contours below 1549.0 nm, a bright large-area contour corresponding to the flat band at 1548.5 nm, and dark contours above 1549.0 nm. The resonance-trapped PhC design also supports quasi-TE resonances; however, near the Dirac

point wavelength of 1548.0 nm we observe high Q -factors and dim scattering contours (Figure 4c,d). For the symmetry-protected PhC, the resonances are quasi-TM and the Q -factor peaks sharply near the Dirac point wavelength of 1558.0 nm (Figure 4e). The experimental images (Figure 4f) show darker contours as the wavelength increases from 1530.0 to 1555.0 nm, indicating progressively smaller radiative losses. Within experimental resolution, we do not observe a bandgap in our devices. At the Dirac point wavelength of 1558.0 nm, we observe minimal scattered intensity at the center of the Fourier plane, indicating the presence of a low-loss mode at the Γ -point. The off-centered bright scattered intensity corresponds to a lower- Q flat band. For wavelengths greater than 1558.0, the contour becomes bright again in good agreement with our numerical calculations.

To measure the Q -factor of the devices, we placed a pinhole in the Fourier plane following lens L3 in Figure 3c. The diameter of the pinhole is 200 μm , yielding a momentum resolution of $\delta \sim 0.002$. The pinhole is mounted on a 2-axis stage to select specific k -points of the iso-frequency contours. We direct the light passing through the pinhole to a photodiode. The photodiode is connected to a lock-in amplifier which is synchronized with a 1 kHz chopper placed in the incident laser beam. We then record the scattered light intensity from the lock-in amplifier, sweeping the laser wavelength, and varying the pinhole position to obtain the Q -factor at various k -values (see Supporting Information, Table 1). The normalized intensity measurements for the lossy, resonance-trapped, and symmetry-protected PhC

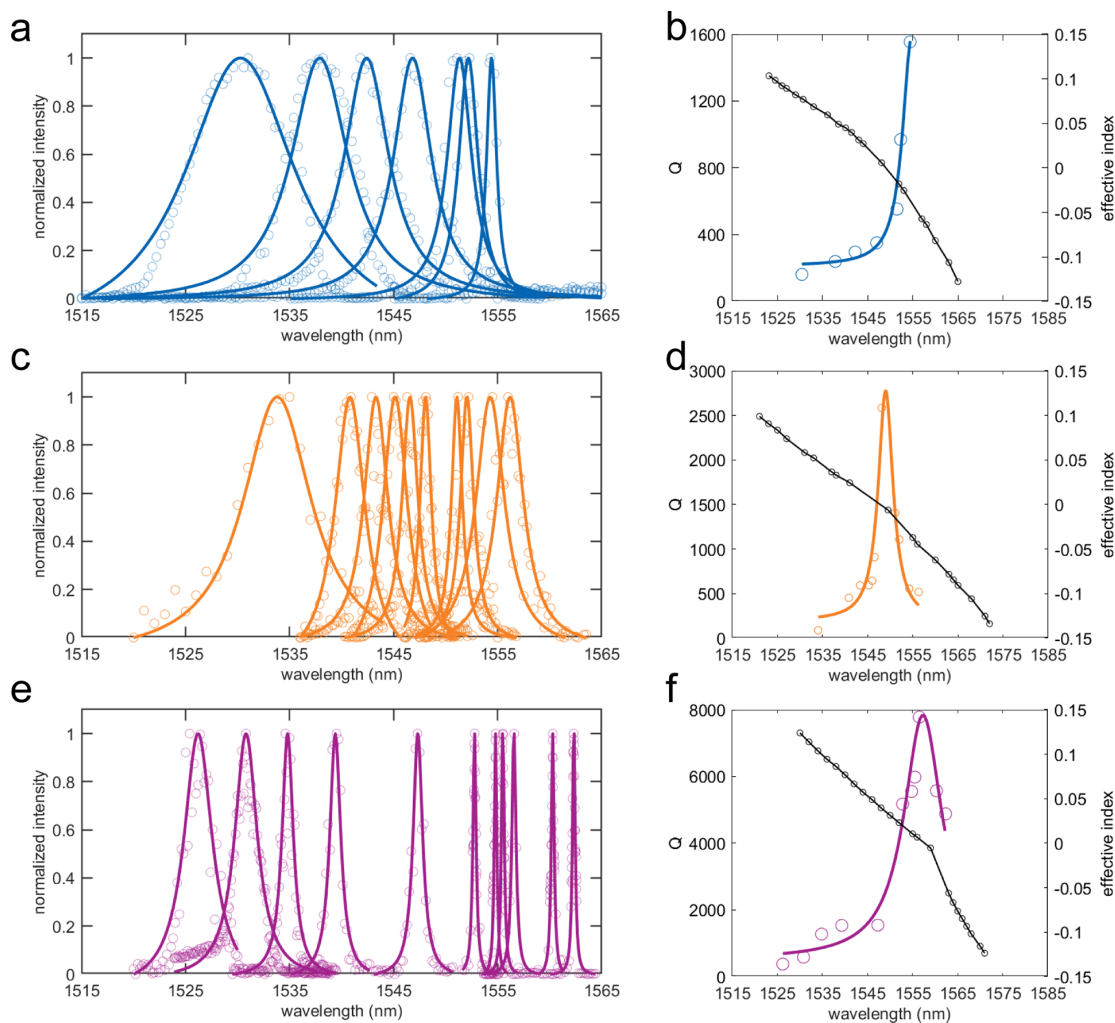


Figure 5. Quality factor measurement. Lorentzian fits to the wavelength-dependence of the normalized scattered-light intensity (a,c,e); each curve represents a different pinhole position and therefore a different k -vector. The Q -factors (left vertical axis of b,d,f) are obtained from the Lorentzian line widths on the left. The effective indices (right vertical axis of b,d,f) are determined from the measured iso-frequency contour. (a,b) Lossy, (c,d) resonance-trapped, (e,f) and symmetry-protected PhC.

designs are shown in Figure 5a,c,e, respectively, and the data collected at a particular k -point is fitted with a Lorentzian. In Figure 5b,d,f, the total Q -factors on the left vertical axis correspond to the full width at half-maximum of the Lorentzians. The right vertical axis shows the absolute value of the index obtained from the measured contour images (Figure 5b,d,f) using the relationship $n = ck/\omega$. Both momentum resolution and the Q -factor constraint are effectively a measurement of zero refractive indexes near the Dirac-cone; thus we could only measure the refractive index and Q -factor nearest to the Dirac-cone. The continuity of measured contour-derived indexes indicates an absence of bandgap. Our index retrieval simulations indicate negative indexes at larger wavelengths (see Supporting Information Figure S6). For the lossy PhC design (Figure 5a,b), we find a Q -factor of 446.6 at the near-zero-index wavelength of 1549.0 nm. At longer wavelength, the Q -factor substantially increases due to a higher- Q off- Γ mode (Figure 1b). The resonance-trapped PhC (Figure 5c,d) has a Q -factor of 2.6×10^3 at a

near-zero-index wavelength of 1548.1 nm, while the symmetry-protected PhC (Figure 5e,f) has a Q -factor of 7.8×10^3 at a near-zero-index wavelength of 1557.0 nm. A slight mismatch with the maximum Q -factor and the zero-index wavelength is attributed to fabrication imperfections. The propagation length is proportional to the group index (n_g) and inversely proportional to the Q -factor, that is, $L \sim n_g/Q$.²⁶ Assuming a constant group index (see Supporting Information Figure S6), we expect an approximate order-of-magnitude improvement. We performed numerical simulations to measure the expected improvement in propagation length (see Supporting Information Figure S8). The results for the resonance-trapped and symmetry-protected PhC design are nearly an order-of-magnitude improvement over the lossy PhC design.

The measured Q -factors are lower than the calculated ones because of the finite size of the device and fabrication disorder (see Supporting Information Figure S9). The finite-size of the patterned area breaks the periodicity of the crystal, and Bloch's theorem is no longer valid in a single unit-cell. However, if we

treat the device as periodic over the length scale of the device and assume a random distribution of disorder, then we can expand the device's supercell mode over the Bloch modes of an ideal photonic crystal evaluated at the fractional orders of the wavevector.^{29,30} For the zero-index mode at the Γ -point, the supercell mode of our photonic crystal designs contains off- Γ , fractional modes with finite Q -factors, and the total Q -factor is reduced. Our experimental results could therefore be improved by increasing the device area and reducing fabrication disorder. Radiation leakage into the silicon oxide substrate also decreases the measured Q -factors. This loss could be mitigated by using an index-matching layer or suspending the devices to create a symmetric index profile in the out-of-plane mirror direction (see Supporting Information Figure S10).

In conclusion, we demonstrated two approaches to mitigate radiative losses in near-infrared zero-index photonic crystals. We experimentally demonstrated an order of magnitude increase in the total quality factor over previous designs and therefore a 10-fold reduction in loss. The symmetry-protected PhC design has a better performance than the resonance-trapped design in reducing the optical losses. Losses could be further reduced by improving fabrication and the index profile. The low-loss zero-index photonic crystal designs we present support on-chip operation, impedance matching, and scalability across the visible and infrared spectrum, given the appropriate high-index dielectric.³¹ These attributes are beneficial for zero-index applications which require low loss and long propagation length scales, such as enhanced nonlinear and quantum interactions in photonic integrated circuits. Our findings open novel routes for the development of on-chip zero-index devices and applications which have so far remained elusive due to the large losses in current designs.

MATERIALS AND METHODS

Simulation. The band structures, Q -factor, and isofrequency contours were computed using three-dimensional finite element method simulations (COMSOL Multiphysics 5.4). We first calculated all the modes in a PhC unit cell with Floquet periodic boundary conditions in the two lattice-vector directions and perfectly matched layers at the boundaries in the out-of-plane direction. TM/TE-polarized modes were selected by evaluating the energy ratio of the electric and magnetic fields in all directions. The field profile, effective index and impedance, propagation loss, and Fano resonance were computed using 3D finite-difference time-domain simulator (Lumerical FDTD).

Sample Fabrication. All devices were fabricated on 220 nm SOI wafers. Using low growth rate PECVD, we deposited additional amorphous silicon to obtain the required thicknesses for the resonance-trapped PhC (570 nm) and symmetry-protected PhC devices (370 nm). To remove the oxide and enhance Si quality, we treated the wafer using RCA cleaning processes. The wafer was then coated with the positive photoresist (ZEP520A) for e-beam writing, followed by reactive ion-beam etching. The positive photoresist was removed afterward.

ASSOCIATED CONTENT

Supporting Information

The Supporting Information is available free of charge at <https://pubs.acs.org/doi/10.1021/acs.nanolett.0c03575>.

Create a Dirac-cone triply degeneracy; modes in Dirac-cone triply degeneracy; tunable resonance-trapped ZIM PhC; resonance-trapped mode; vanishing line width in transmission spectra; effective index, effective impedance and group index; out-of-plane and in-plane schematics; temporal coupled mode theory: line shape of the quality factor; measurement method; propagation loss; disorder characterization; bound states in the continuum (BIC) property in PhC slab with out-of-plane mirror symmetry; angle-resolved transmission/reflection spectra of out-of-plane incidence on PhC slabs; pinhole location (PDF)

AUTHOR INFORMATION

Corresponding Authors

Eric Mazur – School of Engineering and Applied Sciences, Harvard University, Cambridge, Massachusetts 02138, United States; orcid.org/0000-0003-3194-9836; Email: mazur@seas.harvard.edu

Yang Li – Department of Precision Instrument, Tsinghua University, Haidian, Beijing 100084, China; Email: yli9003@mail.tsinghua.edu.cn

Authors

Haoning Tang – School of Engineering and Applied Sciences, Harvard University, Cambridge, Massachusetts 02138, United States; orcid.org/0000-0001-7910-5128

Clayton DeVault – School of Engineering and Applied Sciences, Harvard University, Cambridge, Massachusetts 02138, United States

Sarah Alejandra Camayd-Muñoz – School of Engineering and Applied Sciences, Harvard University, Cambridge, Massachusetts 02138, United States

Yueyang Liu – Department of Precision Instrument, Tsinghua University, Haidian, Beijing 100084, China

Danchen Jia – Department of Optical Engineering Zhejiang University, Hangzhou, Zhejiang 310027, China

Fan Du – School of Engineering and Applied Sciences, Harvard University, Cambridge, Massachusetts 02138, United States

Olivia Mello – School of Engineering and Applied Sciences, Harvard University, Cambridge, Massachusetts 02138, United States

Daryl I. Vulis – School of Engineering and Applied Sciences, Harvard University, Cambridge, Massachusetts 02138, United States

Complete contact information is available at: <https://pubs.acs.org/doi/10.1021/acs.nanolett.0c03575>

Author Contributions

[†]H.T. and C.D. contributed equally to this work.

Author Contributions

S.M. provided the idea of resonance-trapped PhC for this work. H.T., Y.Y.L., Y.L., C.D., D.F., and O.M. carried out the simulations. D.V. provided the initial design of resonance-trapped ZIM and performed initial calculations and experiments. H.T. designed and fabricated the samples. H.T., C.D., and D.J. carried out the measurements. H.T. and D.J. analyzed the experimental results. Y.L. and E.M. supervised the research and the development of the manuscript. H.T. and C.D. wrote the manuscript with input from all authors. All authors

subsequently took part in the revision process and approved the final copy of the manuscript.

Notes

The authors declare no competing financial interest.

ACKNOWLEDGMENTS

The authors thank Yi Yang, Chao Peng, Renjing Xu, Orad Reshef, Carlos Rio, Meng Xiao, Shahin Firuzi, and Tian Dong for discussions. The Harvard University team acknowledges support from DARPA under contract URFAO: GR510802 for the optical characterization, numerical simulations, and device fabrication described in this paper. The sample fabrication was performed at Harvard University's Center for Nanoscale Systems, which is a member of the National Nanotechnology Coordinated Infrastructure Network and is supported by the National Science Foundation under NSF award 1541959.

REFERENCES

- (1) Adams, D. C.; Inampudi, S.; Ribaudo, T.; Slocum, D.; Vangala, S.; Kuhta, N. A.; Goodhue, W. D.; Podolskiy, V. A.; Wasserman, D. Funneling light through a subwavelength aperture with epsilon-near-zero materials. *Phys. Rev. Lett.* **2011**, *107*, 1–5.
- (2) Silveirinha, M.; Engheta, N. Tunneling of Electromagnetic Energy through Subwavelength Channels and Bends using ϵ -Near-Zero Materials. *Phys. Rev. Lett.* **2006**, *97*, 157403.
- (3) Suchowski, H.; et al. Phase Mismatch - Free Nonlinear Propagation in Optical Zero-Index Materials. *Science (Washington, DC, U. S.)* **2013**, *342*, 1223–1226.
- (4) Caspani, L. Enhanced Nonlinear Refractive Index in ϵ -Near-Zero Materials. *Phys. Rev. Lett.* **2016**, *116*, 233901.
- (5) Alam, M. Z.; De Leon, I.; Boyd, R. W. Large optical nonlinearity of indium tin oxide in its epsilon-near-zero region. *Science (Washington, DC, U. S.)* **2016**, *352*, 795–797.
- (6) Bruno, V.; et al. Negative Refraction in Time-Varying Strongly Coupled Plasmonic-Antenna-Epsilon-Near-Zero Systems. *Phys. Rev. Lett.* **2020**, *124* (4), 043902.
- (7) Khurgin, J. B.; et al. Adiabatic frequency shifting in epsilon-near-zero materials: the role of group velocity. *Optica* **2020**, *7* (3), 226–231.
- (8) Reshef, O.; et al. Beyond the perturbative description of the nonlinear optical response of low-index materials. *Opt. Lett.* **2017**, *42*, 3225.
- (9) Vertchenko, L.; Akopian, N.; Lavrinenko, A. V. Epsilon-Near-Zero Grids for On-chip Quantum Networks. *Sci. Rep.* **2019**, *9* (1), 1–7.
- (10) Liberal, I.; Engheta, N. Zero-index structures as an alternative platform for quantum optics. *Proc. Natl. Acad. Sci. U. S. A.* **2017**, *114*, 822–827.
- (11) Kinsey, N.; DeVault, C.; Boltasseva, A.; Shalae, V. M. Near-zero-index materials for photonics. *Nature Reviews Materials* **2019**, *4*, 742–760.
- (12) Liberal, I.; Engheta, N. Near-zero refractive index photonics. *Nat. Photonics* **2017**, *11*, 149–158.
- (13) Huang, X.; Lai, Y.; Hang, Z. H.; Zheng, H.; Chan, C. T. Dirac cones induced by accidental degeneracy in photonic crystals and zero-refractive-index materials. *Nat. Mater.* **2011**, *10* (8), 582–586.
- (14) Li, Y.; et al. On-chip zero-index metamaterials. *Nat. Photonics* **2015**, *9*, 738–742.
- (15) Vulis, D. I.; et al. Monolithic CMOS-compatible zero-index metamaterials. *Opt. Express* **2017**, *25* (11), 12381–12399.
- (16) Suchowski, H.; et al. Phase mismatch-free nonlinear propagation in optical zero-index materials. *Science* **2013**, *342* (6163), 1223–1226.
- (17) Reshef, O.; De Leon, I.; Alam, M. Z.; Boyd, R. W. Nonlinear optical effects in epsilon-near-zero media. *Nature Reviews Materials* **2019**, *4* (8), 535–551.
- (18) Sakoda, K. Proof of the universality of mode symmetries in creating photonic Dirac cones. *Opt. Express* **2012**, *20* (22), 25181.
- (19) Friedrich, H.; Wintgen, D. Interfering resonances and bound states in the continuum. *Phys. Rev. A: At, Mol, Opt. Phys.* **1985**, *32* (6), 3231.
- (20) Kodigala, A.; Lepetit, T.; Gu, Q.; Bahari, B.; Fainman, Y.; Kante, B.; et al. Lasing action from photonic bound states in continuum. *Nature* **2017**, *541* (6), 196–199.
- (21) Yang, Y.; Peng, C.; Liang, Y.; Li, Z.; Noda, S. Analytical perspective for bound states in the continuum in photonic crystal slabs. *Phys. Rev. Lett.* **2014**, *113* (3), 037401.
- (22) Hsu, C. W.; Zhen, B.; Stone, A. D.; Joannopoulos, J. D.; Soljacic, M. Bound states in the continuum. *Nature Reviews Materials* **2016**, *1* (9), 1–13.
- (23) Sadrieva, Z. F.; et al. Transition from Optical Bound States in the Continuum to Leaky Resonances: Role of Substrate and Roughness. *ACS Photonics* **2017**, *4* (4), 723–727.
- (24) Hsu, C. W.; et al. Observation of trapped light within the radiation continuum. *Nature* **2013**, *499*, 188–191.
- (25) Gansch, R.; Kalchmair, S.; Genevet, P.; Zederbauer, T.; Detz, H.; Andrews, A. M.; Schrenk, W.; Capasso, F.; Loncar, M.; Strasser, G. Measurement of bound states in the continuum by a detector embedded in a photonic crystal. *Light: Sci. Appl.* **2016**, *5* (9), No. e16147.
- (26) Minkov, M.; Williamson, I. A. D.; Xiao, M.; Fan, S. Zero-Index Bound States in the Continuum. *Phys. Rev. Lett.* **2018**, *121* (26), 263901.
- (27) Sakoda, K. *Optical properties of photonic crystals*; Springer series in optical sciences; Springer, 2001, Vol. 80.
- (28) Regan, E. C.; et al. Direct imaging of isofrequency contours in photonic structures. *Sci. Adv.* **2016**, *2* (11), No. e1601591.
- (29) Wang, Z.; et al. Mode splitting in high-index-contrast grating with mini-scale finite size. *Opt. Lett.* **2016**, *41* (16), 3872–3875.
- (30) Jin, J.; et al. Topologically enabled ultrahigh-Q guided resonances robust to out-of-plane scattering. *Nature* **2019**, *574* (7779), 501–504.
- (31) Chen, W. T.; et al. A broadband achromatic metalens for focusing and imaging in the visible. *Nat. Nanotechnol.* **2018**, *13* (3), 220–226.